communications physics

Article

https://doi.org/10.1038/s42005-024-01882-5

Modified Born series with virtual absorbing boundary enabling large-scale electromagnetic simulation

Check for updates

Pinxuan He[1], Jiamin Liu[1] ✉, Honggang Gu[1,2], Hao Jiang[1] & Shiyuan Liu[1,3] ✉

Numerical electromagnetic field solvers are significant for nanophotonic and photoelectronic technology, especially for computational imaging, metasurface, and biomedical microscopy, in which large-scale simulations serve as the core. Conventionally, these simulations use absorbing boundary conditions (ABC) to simulate open-domain systems. However, the existing ABCs require large memory to sufficiently suppress reflection at boundaries, which is prohibitive for large-scale applications. This work proposes a virtual absorbing boundary condition based on the angular spectrum method (ASM) to reduce the memory usage of ABC. The ASM is used to cover the polluted field in the boundary region, which eliminates the need to store the field in the boundary region. Combined with the Fourier transforms-based modified Born series, memory usage can be reduced to a level close to the theoretical limit. This proposed method offers a substantial boost for applications related to large-scale simulations and memory-constrained devices like GPU.

Large-scale simulations of light propagation in complex structured media are essential in many fields of optics[1–3]. There are many classical methods, including finite-difference time-domain (FDTD)[4,5], finite-difference frequency-domain[6,7], modified Born series (MBS)[8,9], and finite element method[10], which can conduct rigorous simulations by solving Maxwell Equations. For large-scale simulations with dimensions in the scale of thousands of wavelengths, such as metasurface design[11], biology imaging[12–14], and lithography simulations[15], the memory requirement is the bottleneck for all numerical simulators mentioned above[16]. Therefore, it is essential to reduce memory consumption to ensure the feasibility of large-scale simulations.

In most situations of interest, one usually needs to simulate a non-periodic domain with scatter inside[17,18]. In these scenarios, absorbing boundary conditions (ABC) are applied to surround the region of interest (ROI) with the aim of absorbing the outgoing light. For qualified ABCs, it is necessary to achieve both low reflection and transmission simultaneously. Low reflection is attainable when the variation of the refractive index (RI) in the boundary region is smooth enough. Provided that the RI changes smoothly, a thick boundary is required to get low transmission. In other words, a large amount of memory is often occupied by the ABCs.

The most well-known and widely applied ABC is the perfectly matched layer (PML)[19,20]. Although the PML is more powerful than other contemporary methods[21], it still requires significant thickness to achieve accurate simulations. Moreover, the PML introduces non-uniform permeability[20,22], which exacerbates the computational requirement and is unnecessary for many applications. Like the PML, the polynomial boundary layer (PBL)[9] absorbs light by gradually varying RI, while it does not exploit the permeability and is inferior to the PML. The anti-reflection boundary layer (ARL)[23] is an effective ABC based on window functions, while it is optimized for special situations and its performance may be unstable. The acyclic convolution (ACC) is an auxiliary method for improving the performance of the ABCs[23]. Even with the help of the ACC, the boundary region occupies a significant amount of memory to ensure good performance.

We propose a virtual boundary condition (VBC) to reduce the memory usage of the ABCs, which is inspired by the parallel strategy of the FDTD[24] and the pseudo propagation in the MBS method[9]. In the FDTD method, the field is updated iteratively based on the adjacent field of the last time step. If there is any error in the simulation domain, the error propagation is limited by the number of iterations. The MBS method is a frequency domain method and does not have physical propagation in the time domain. However, there is a pseudo propagation shown in Fig. 1a, which results from the localized dyadic Green's function in the MBS method. λ represents the vacuum wavelength. The Green's function used in the MBS method is

[1]State Key Laboratory of Intelligent Manufacturing Equipment and Technology, Huazhong University of Science and Technology, Luoyu Road, Wuhan, 430074 Hubei, China. [2]Guangdong HUST Industrial Technology Research Institute, Guangdong Provincial Key Laboratory of Manufacturing Equipment Digitization, Dongguan, 523003 Guangdong, China. [3]Optics Valley Laboratory, Wuhan, 430074 Hubei, China. ✉e-mail: jiaminliu@hust.edu.cn; shyliu@hust.edu.cn

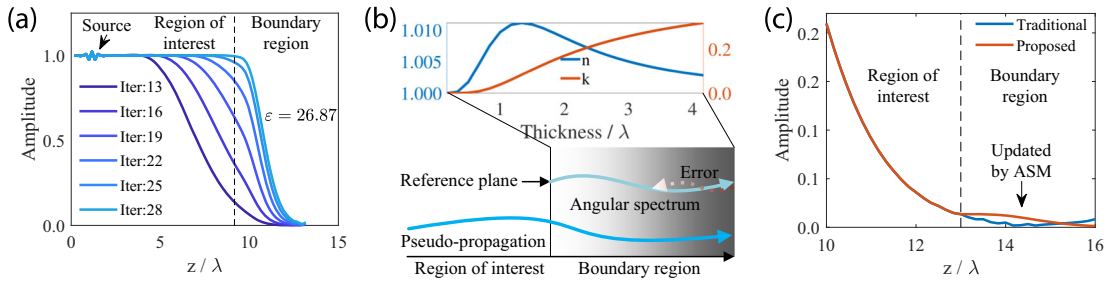

Fig. 1 | Schematic diagram of the virtual boundary condition. a The amplitude of the electric field of different iterations for the simulation of plane wave propagation by the modified Born series. The field is propagated from the source position and absorbed in the boundary region. λ represents the vacuum wavelength. The damping factor ε is 26.87 in this example. **b** The basic idea of the virtual boundary condition. The field in the absorbing boundary region, which is generated by pseudo propagation and may contain errors, is recalculated with the angular spectrum method (ASM). The inset shows a typical complex refractive index, $n + ik$, defined by the polynomial boundary layer. The introduced absorption improves the performance of the virtual boundary condition. **c** The amplitude of field updated by the ASM. The unwanted fluctuation of the field magnitude in the boundary region stemming from insufficient absorption is covered by the ASM.

shown as follows,

$$\mathbf{g}(\mathbf{r}) = \mathbf{C}\frac{e^{\mathrm{i}\sqrt{k_0^2+\mathrm{i}\varepsilon}|\mathbf{r}|}}{4\pi|\mathbf{r}|}, \tag{1}$$

where k_0 represents background wavenumber. i is the imaginary unit. $\mathbf{C}$ is a 3×3 matrix describing the conversion between different polarizations, which can be expressed as $\mathbf{C} = \mathrm{I} + \nabla\nabla^{\mathrm{T}}/k_0^2$[25]. The damping factor ε controls the speed of the pseudo propagation and needs to be greater than or equal to $\max_{\mathbf{r}}|k(\mathbf{r})^2 - k_0^2|$ to ensure the convergence[9], where $k(\mathbf{r})$ is the wavenumber. The corresponding ε in Fig. 1a is 26.87. Note that the result of the MBS method is independent of the localization feature of Green's function. Details regarding the Green's function have been discussed in previous work[25].

Based on the concept of the pseudo propagation, the VBC uses the angular spectrum method (ASM) to eliminate the boundary artifacts caused by insufficient absorption, as shown in Fig. 1b. The typical RI inside the boundary region is shown in the inset of Fig. 1b, which is calculated by the PBL with N = 5 and $\max_{\mathbf{r}}|k^2(\mathbf{r}) - k_0^2| = 1$[9]. Both the absorption in the boundary region and the localization in Eq. (1) are utilized to achieve zero reflection. In this framework, errors in the boundary region are tolerable, as illustrated in Fig. 1c. Therefore, the required thickness of the ABCs can be reduced. Considering that the field in the boundary region is recalculated in each iteration, there is no need to store these data, which can further reduce memory usage. Three examples, including the propagation of a single plane wave, the diffraction of the EUVL mask, and the scattering of biological cells, are provided to demonstrate the performance of the proposed method.

Results

Virtual boundary condition

The MBS method[8,9,22,26], is a frequency domain method widely applied to optical diffraction tomography[27], extreme ultraviolet mask near-field calculation[28,29], and inverse scattering problem[25]. The MBS method solves the Maxwell equations iteratively as

$$\mathbf{E}_{n+1} = \boldsymbol{\gamma}\mathbf{G}\mathbf{E}_n{}' + (1-\boldsymbol{\gamma})\mathbf{E}_n, \tag{2}$$

where

$$\mathbf{E}_n{}' = \mathbf{V}\mathbf{E}_n + \mathbf{S}, \tag{3}$$

$$\boldsymbol{\gamma} = \mathrm{i}\mathbf{V}/\varepsilon. \tag{4}$$

Here, $\mathbf{E}_n$ is a vector containing the fields from the last iteration. $\mathbf{V}$ is a diagonal matrix containing the scattering potential determined by the RI. $\mathbf{S}$ is a vector containing the source term. Note that for general ABCs, these matrices and vectors store not only the data inside the ROI but also that in the boundary region throughout the calculation, as shown in Fig. 2a. $\mathbf{G}$ represents the convolution with the Green's function, which is the only operator responsible for the propagation in the general MBS method. $\mathbf{G}$ is conducted by the Fourier transforms.

$$\mathbf{G}\mathbf{E}_n{}' = F_{3\mathrm{D}}^{-1}\{F_{3\mathrm{D}}\{\mathbf{E}_n{}'\} \cdot \mathbf{g}(\mathbf{k})\}, \tag{5}$$

where $F_{3\mathrm{D}}$ and $F_{3\mathrm{D}}^{-1}$ represent the 3D forward and inverse FFTs, respectively. $\mathbf{g}(\mathbf{k})$ is the frequency-domain Green's function.

The standard calculation process of the convolution is shown in Fig. 2a. The blue array represents the field inside ROI in the space domain. The red one represents that in the frequency domain. The gray arrays represent the field in the boundary region. N_x, N_y, and N_z are the data sizes in corresponding directions. In the traditional implementation of the convolution, the three-dimension (3D) data is converted to the frequency domain by 3D fast Fourier transforms (FFT) and multiplied with the Green's function.

For the convolution with the VBC in Fig. 2b, the data in the boundary region can be calculated by the ASM. The 3D FFT is decomposed into a 2D FFT on the x- and y-axes and a 1D FFT on the z-axis to conduct the ASM. Although the ASM is designed to calculate the propagation in a homogeneous medium, it can be adopted here without sacrificing accuracy due to the smooth variation of the RI inside the boundary region shown in the inset of Fig. 1b. The ASM is used to propagate the field based on the field at the reference plane. Although $\mathbf{E}_n{}'$ does not represent the field and cannot be propagated by the ASM in theory, it is equivalent to applying the ASM on $\mathbf{E}_n$ and then calculating $\mathbf{E}_n{}'$ as long as the RI of the reference plane is uniform and there is no source term at the reference plane.

It is noted that the operations between the 2D FFT, including the ASM propagation, 1D FFT, and multiplication, can be decoupled in the x- and y-axes. Therefore, the data is extracted and operated in the depth direction, as shown in Fig. 2c, which avoids dealing with large and bulky data. The memory required by the decoupled VBC can be compressed to a negligible level compared with that of traditional ABCs.

The ASM is a classical method for modeling the light propagation in homogeneous media, which can be expressed as

$$E(x,y,z) = F_{2\mathrm{D}}^{-1}\{F_{2\mathrm{D}}\{E(x,y,z_{\mathrm{ref}})\}p(z)\}, \tag{6}$$

where

$$p(z) = \exp\left(1\mathrm{i} \times (z - z_{\mathrm{ref}}) \times \sqrt{\left(k_0 n_{\mathrm{bg}}\right)^2 - k_x^2 - k_y^2}\right). \tag{7}$$

Here $F_{2\mathrm{D}}$ and $F_{2\mathrm{D}}^{-1}$ represent the 2D forward and inverse Fourier transforms (FFT), respectively. $p(z)$ is the transfer function. z_{ref} is the z coordinate of reference plane. k_0 is the free-space wave vector. k_x and k_y are the spatial

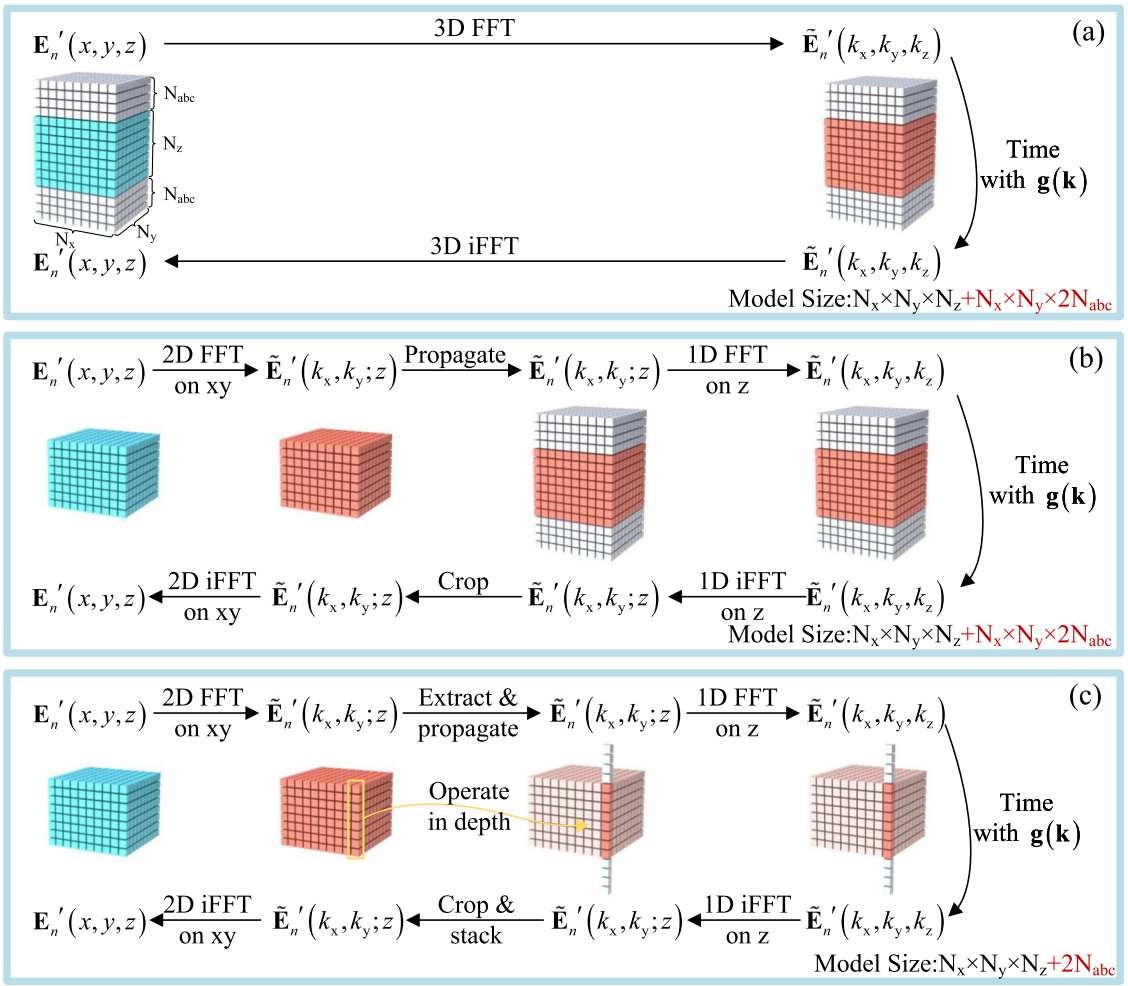

Fig. 2 | The schematic diagram of the implementation of the virtual boundary condition. a Implementation of the conventional operation. First, the data is converted into the frequency domain. Then, the data is multiplied by the Green's function and converted back. **b** Implementation with the virtual boundary condition. The 3D FFT is decomposed into 2D FFT and 1D FFT. The data in the absorbing boundary region is generated entirely by the angular spectrum method. **c** Implementation with decoupled virtual boundary condition. After the 2D FFT, the operation can be decoupled in the x- and y-axes. Therefore, the data in the absorbing boundary region can be operated on a minimal scale, which allows almost zero memory consumption at the boundary.

frequency coordinates. n_{bg} is the background RI of medium. Both Eqs. (1) and (7) describe the wave propagation in the frequency domain. The former is based on spherical waves, while the latter is based on plane waves.

The propagation with Eq. (6) needs to take the square root for all layers in the boundary region, which is cumbersome. Note that the RI of the whole boundary is close to the RI of the first layer of the boundary. Besides, the field's energy concentrates on the low-frequency part in most simulations. Therefore, the transfer function in Eq. (7) can be discretized and simplified as,

$$p(z) = \exp\left(1\mathrm{i} \times N(z) \times \sqrt{k_0^2 - \left(\frac{k_x}{n(z_1)}\right)^2 - \left(\frac{k_y}{n(z_1)}\right)^2}\right), \quad (8)$$

where

$$N(z) = \sum_{z_t=z_1}^{z} \Delta z \times n(z_t). \quad (9)$$

Here Δz is the grid size in the z-direction. z_1 is the z coordinate of the first layer after the reference layer. $n(z_t)$ represents the varying RI determined by the underlying boundary condition. This simplification can avoid calculating the square root repeatedly.

Besides the benefit of memory usage, the computational complexity of the VBC is smaller than that of the conventional one. From the view of computation, the VBC avoids 2D FFT on the boundary region, while only an extra evaluation of the exponential function on Eq. (8) is needed. The computational complexity of performing a 2D FFT on the x- and y-axes of an $N_x \times N_y \times N_{abc}$ array is $O(N_{abc}N_xN_y \log(N_xN_y))$. In contrast, computing the exponential function for every element in the array has a complexity of $O(N_{abc}N_xN_y)$, as it only involves a constant-time operation per element. Thus, the 2D Fourier transform is more computationally intensive due to the logarithmic factor, making the VBC generally more efficient, especially for large N_x and N_y.

The VBC is solely applied to one axis in this work, which is acceptable because the source in most large-scale simulations is directional. The outgoing light in other directions is minimal, and other ABCs with a thin thickness can be used. The VBC is compatible with other boundary conditions like the PBL and ARL, except for the ACC, as the ACC is based on an accumulative solution in which errors during iterations are not permitted[23]. The VBC can be applied to all three axes. As a result, the ASM cannot be performed within the convolution of the MBS method. Instead, the ASM is conducted on all axes independently and sequentially. Bulky memory is allocated to store the data in the boundary region. Even though the memory requirement remains lower because the boundary region only exists in one variable $\mathbf{E}_n'$ instead of several

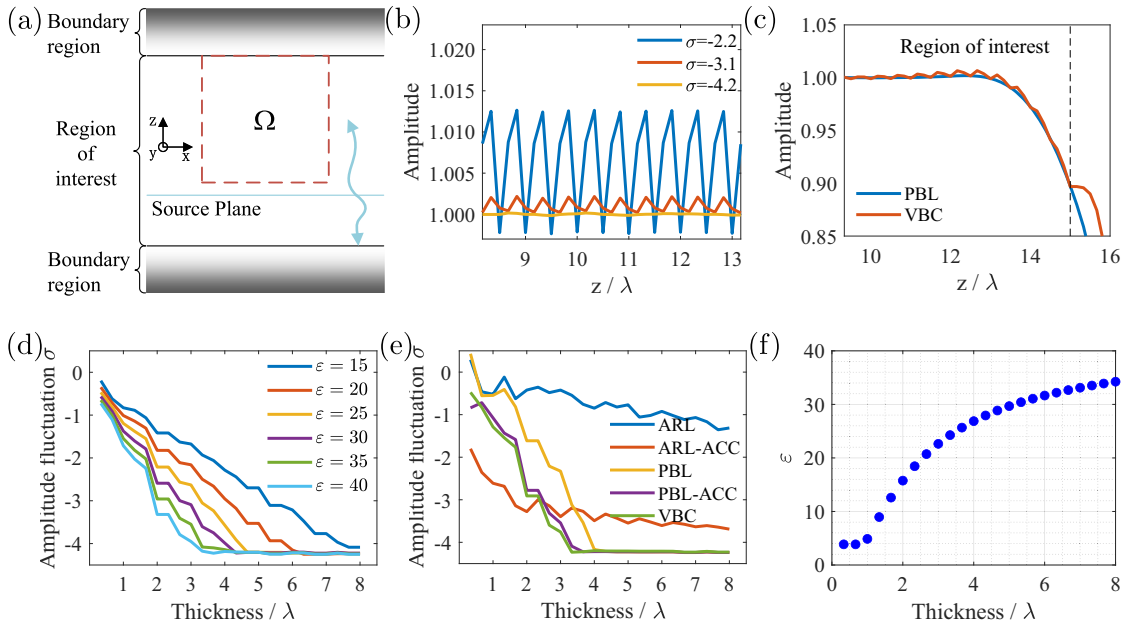

Fig. 3 | Plane wave propagation simulations without scatter. a The illustration of the simulation configuration. The source is normally incident along the z-axis. Ω is a subregion within the region of interest. The amplitude fluctuation σ is defined as the standard deviation of the field's amplitude within the region Ω. Lower σ means better performance. **b** Examples of the amplitude with various σ. **c** The temporary reflection that occurs during the iterations with the virtual boundary condition. **d** The performance comparison for the virtual boundary condition with different ε. **e** The performance comparison for various boundary condtions. A comprehensive definition of the polynomial boundary layer (PBL), anti-reflection boundary layer (ARL), and acyclic convolution (ACC) is available in previous literature[9,23]. **f** The corresponding ε for the PBL with various thicknesses. The PBL is a classical absorbing boundary condition that applies a varying refractive index. The damping factor ε controls the speed of the pseudo propagation and is constrained by the refractive index in simulation region.

variables including $\mathbf{V}$, $\mathbf{E}_n$, and $\mathbf{E}_n'$, it is not recommended due to the complex implementation.

Propagation of plane wave

To validate the performance of the VBC, the simulations of normal-incident light propagation in free space with various ABCs were conducted. The simulation configuration is shown in Fig. 3a. If there is any reflection of fields caused by the ABCs, the reflected fields interfere with the incident fields. The greater the interference, the more pronounced the fluctuation in the field amplitude. Because of the periodic nature of the discrete Fourier transform, there may be unabsorbed light from adjacent periods, which also leads to amplitude fluctuation. Therefore, the performance of the ABCs can be directly evaluated by the amplitude fluctuation σ, which is defined as the standard deviation of the amplitude of fields,

$$\sigma = \log_{10}\sqrt{\frac{1}{|\Omega|}\sum_{(x,y,z)\in\Omega}\left(|E_y(x,y,z)| - \mu\right)^2} \quad \text{with} \quad \mu = \frac{1}{|\Omega|}\sum_{(x,y,z)\in\Omega}|E_y(x,y,z)|, \tag{10}$$

where Ω is a region inside the ROI, as indicated in Fig. 3a. Different levels of amplitude fluctuations are shown in Fig. 3b. During the iterations with the VBC, a small reflection can be found near the interface between the ROI and boundary region, as shown in Fig. 3b. The reflection is caused by the temporary discontinuous derivative of the field, and it will be repaired in the later iterations, as implied by the small σ.

The VBC can be implemented without underlying ABCs, in which case its effectiveness depends on ε. The larger ε leads to shorter propagation length and better absorption. The performance of the VBC with different ε is shown in Fig. 3d. The results align well with expectations. Generally, the amplitude fluctuation σ declines with increasing thickness and converges to a stable value. Small ε needs a thick boundary to ensure absorption, while large ε slows down the convergence of the simulations. Fortunately, the VBC can be implemented upon the PBL. After the absorption by the PBL, the amplitude of the errors can be suppressed. In other words, the error occurring at the outermost layer of the whole simulation can be limited by the localization of the Green's function and lowered by the absorption in the boundary region.

The performance of the VBC with enhancement from the PBL is compared to other existing ABCs, as shown in Fig. 3e. A comprehensive definition of the PBL, ARL, and ACC is available in previous literature[9,23]. Although the PBL with increasing thickness will result in a larger RI difference and higher ε in this example, as depicted in Fig. 3f, there is still apparent performance enhancement. For example, the σ of the enhanced VBC attains its lowest value with a thickness of 3.33λ. The corresponding ε is approximately 25, while the σ of the original VBC at the same ε reaches its minimum point with a thickness of 4.66λ. Therefore, the VBC in this work is implemented upon the PBL by default. Compared to the other ABCs, the decay of σ with the enhanced VBC is faster, and the required thickness to reach the lowest σ is the smallest. It is shown that the performance of the VBC is superior to that of the others, while its memory requirement is negligible.

Diffraction of extreme ultraviolet lithography mask

Extreme ultraviolet lithography (EUVL) mask simulations are necessary for the high-volume manufacturing of the advanced integrated circuit, which enables understanding and compensating the severe thick mask effect[30,31]. Here, the diffraction of the absorber in the EUVL mask is separately simulated by the MBS method[28,29]. The typical thickness of the absorber is 50 nm, while the spans of the ROI in the x- and y-axes are in the order of micrometers. Larger spans are urgently needed to suppress the stitching errors[32]. The simulation region is planar, and the incident light is along the thickness direction, as shown in Fig. 4a. Such planar simulations are typical for large-scale simulations in computational imaging[2,33] and metasurface[34,35], given that most functional optical components are manufactured in 2D.

Taking EUVL mask simulations as an example, only about 44% of the simulation domain is the ROI, and the rest is the boundary region to ensure sufficient absorption. Therefore, it is essential to reduce memory usage and

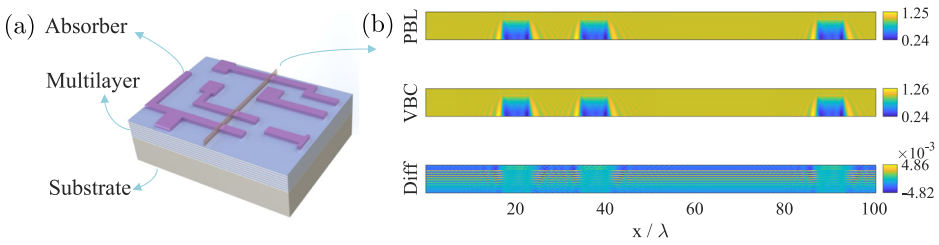

Fig. 4 | Diffraction calculation of extreme ultraviolet lithography mask. a The diagram of the mask, which is a typical planar structure. Usually, the absorber is simulated separately. **b** The amplitude of the field with the polynomial boundary layer (PBL) and virtual boundary condition (VBC). The differences between the two results are shown below. The vertical scale is identical to the horizontal scale. The simulation result is almost identical, while the memory consumption of the VBC is negligible.

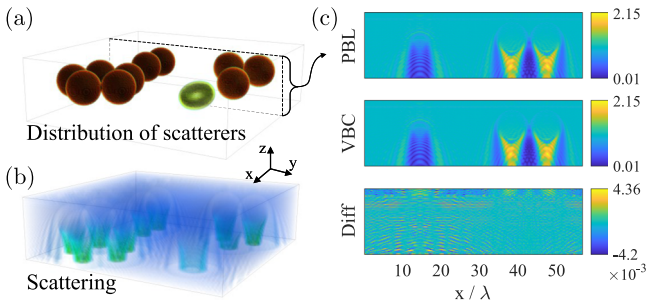

Fig. 5 | Scattering calculation for optical diffraction tomography. a The distribution of the scatterers, including silica microspheres and a live mouse red blood cell. The medium is water. **b** The visualization of the scattering by the samples. **c** A cross-section of the field's amplitude with the polynomial boundary layer (PBL) and virtual boundary condition (VBC). The differences between the two results are shown below. The vertical scale is identical to the horizontal scale. The VBC alleviates memory usage without sacrificing accuracy.

Table 1 | Computational efficiency comparison

Examples	Model reduction rate	Boundary condition	Iterations	Time (s)
Propagation of plane wave	34.78%	PBL	39	1.524
		PBL-ACC	40	1.636
		VBC	39	1.753
Diffraction of EUVL mask	54.54%	PBL	25	8.069
		PBL-ACC	26	8.352
		VBC	25	9.781
Scattering of microspheres	37.04%	PBL	64	2.596
		PBL-ACC	66	2.771
		VBC	65	2.761

The model reduction rate is defined as the reduction in model size due to the adaptation of the virtual boundary condition (VBC) compared to the original one. A comprehensive definition of the polynomial boundary layer (PBL) and acyclic convolution (ACC) is available in previous literature[9,23].

improve the computational feasibility of large-scale simulations. The diffraction of the mask absorber is simulated under different absorbing boundary conditions. The amplitude of the field is shown in Fig. 4b. It can be observed that the result from the VBC is consistent with that from the PBL. The effectiveness of the VBC is validated. The discrete grid on the xy-plane is 1125 × 1000, and the corresponding memory requirement of the VBC can be six orders of magnitudes less than that of the PBL.

Scattering in optical diffraction tomography

Optical diffraction tomography (ODT) is a powerful tool for studying hematology[36,37], morphological parameters[38], and biochemical information[39], which can quantitatively measure the 3D information for non-fluorescent micro-samples. The ODT reconstructs the sample based on multiple 2D measurements from various illumination angles, in which the forward modeling is fundamental for accurate reconstructions. The MBS method is widely applied in the ODT because of its capability to capture multiple scattering effect[25]. With the goal of high-resolution, large field-of-view (FOV) and 3D thick sample, the simulation domain of the ODT and the memory requirement are rapidly increasing[13,25,40,41]. Although the large simulation can be divided into small subsets to reduce memory requirement, the accuracy of the reconstructions may be impaired even with a large overlap between the subsets. The VBC can significantly alleviate memory shortages and make larger simulations possible for the ODT.

The simulation of silica microspheres and a live mouse red blood cell in water is shown in Fig. 5. Unlike the previous examples, the scattered field of the microspheres contains more high-frequency components. Therefore, the approximation in Eq. (8) is not applied. It can be observed that the incident light is strongly scattered, and the field interaction between different samples is considerable with a small distance, which is essential for clearly resolving the cell-cell interaction dynamics. A cross-section of the field's amplitude is depicted in Fig. 5c. With the VBC, these effects can be simulated accurately. In this example, 37.04% of the memory is for the boundary region, which means that the VBC can provide an extra 58.83% of the FOV in the ODT with the same memory consumption.

Discussion

The computational efficiency of the proposed method is evaluated using the three examples presented earlier. The boundary thickness for the plane wave propagation is set to 4λ. Three boundary conditions are compared in Table 1. The model reduction rate is defined as the reduction in model size due to the adaptation of the VBC compared to the original model size. Given that the simulated systems can be compressed up to 54.54%, the computational overhead of the VBC is acceptable in comparison to the original computational cost. The iteration numbers are nearly identical, which is because the ε are the same in all boundary conditions. Although the VBC could accelerate the convergence by propagating the field analytically in the boundary region, there are other factors that influence convergence, including temporary reflection caused by the virtual boundary, diffraction, and scattering inside the system. The MBS method will not converge until all of these phenomena are properly addressed.

The MBS method with the VBC consistently converges in our tests and simulations. This system, distinct from the original MBS method, is subject to continuous external adjustments, which makes the theoretical proof of convergence extremely difficult. Therefore, we analyze the impact of the VBC on the stability of the solution. Even in the worst situations where there some reflection error arrives the reference plane of the VBC, the error inside the boundary region is bigger than the one at the reference plane. The VBC will replace the big error with the small one through the boundary region with attenuation, determined by the underlying boundary condition. So, the VBC does not destabilize the solution. The simulation with the VBC is highly likely to converge under sufficient absorption and localization.

Although the proposed method demonstrates excellent absorption performance along a single axis with minimal memory usage, it cannot achieve the same effectiveness when applied simultaneously to multiple axes, as previously mentioned. The ASM in multiple directions cannot be effectively integrated with convolution. If small lateral artifacts are present in the other axes, they can be addressed using the PBL[9] or ARL[23] with small

thickness. However, if there is significant outgoing light in all directions and thin absorbing boundaries are required across all three axes, the ACC[23] is preferred over the proposed method. The results in Table 1 indicate that VBC requires additional computation time, suggesting a trade-off between memory usage and computation time. As shown in Fig. 2, the 3D FFT is replaced by numerous operations in the VBC, which likely contributes to this time difference. This is because the FFT leverages a highly optimized library[42], while the VBC relies on hand-written MATLAB code. We believe that optimizing the code or implementing the VBC using low-level programming techniques could improve efficiency and help mitigate this time-related drawback.

Different from other rigorous methods based on finite differences which require 8 to 10 cells per wavelength at least to avoid unacceptable numerical error[43,44], the MBS method solves the Maxwell equations by the FFT. The required discretization is only 2 cells per wavelength[9,45], which is dictated by the Nyquist sampling theorem. Combined with the proposed VBC, almost all the memory is allocated to the ROI, and the grid size in the ROI can be maximized. The memory usage of the MBS method can be reduced to a level that is close to the theoretical limit, which significantly improves the computational feasibility for large-scale simulations. The VBC can be easily implemented with single instruction/multiple data techniques[46]. For the simulations conducted on graphics processing units (GPU) where the available memory is much smaller than that of central processing units (CPU), it is vital to minimize memory usage. The VBC shows promising potential across a broad spectrum of applications, spanning computational imaging[2], metasurface[11], and biomedical microscopy[12–14].

The viability of the proposed method is based on three assumptions. First, the VBC is limited to frequency domain solvers due to the adoption of the ASM. Second, there is a pseudo propagation during the solving process. Third, the calculation must be iterative, and the next iteration is based on the updated solution.

Besides the MBS method, there are many popular frequency-domain solvers, such as the finite-difference frequency-domain and finite element methods. These methods are formulated as $Ax = b$ and solved by iterative algorithms for large-scale simulations. Usually, A is a large sparse matrix with a small bandwidth, which leads to extremely slow pseudo propagation during the iterations. Taking the finite-difference frequency-domain method as an example, the pseudo propagation speed is one cell per iteration[47], which means that only one layer of the ABC is needed with the VBC. Unfortunately, the application of the VBC is limited by the fact that most modern algorithms for linear equations do not use the updated solution for the next iteration[48]. Therefore, the VBC has the potential to be applied to other methods with competent stationary iterative algorithms.

Methods

The VBC is implemented with Matlab. The computations were carried out on a workstation featuring an Nvidia RTX 5000 GPU with 16 GB of memory, supported by an Intel Xeon Gold 6285R processor with 512 GB of memory. The PBL with $N = 5$ and $\max_{\mathbf{r}}|k^2(\mathbf{r}) - k_0^2| = 1$ is used throughout this work. Although the data of the boundary region is not stored in the MBS method with the VBC, the calculation of ε still takes into account the RI of the boundary region. For the ARL and ACC, we use the default parameters in ref. 23. The default amplitude of the sources is 1. The iteration of the MBS method stopped when the change of the field is less than 0.005 by default.

For the plane wave propagation, the grid size of the simulations is 0.167λ. The ROI of the simulations is $55\lambda \times 55\lambda \times 15\lambda$. The incident field is y-polarized and is located at $z = 4\lambda$. The region Ω is defined as $\{(x, y, z)|x \in [24.167\lambda, 30.833\lambda], y \in [24.167\lambda, 30.833\lambda], z \in [5\lambda, 15\lambda]\}$. All simulations ran for 200 iterations to ensure convergence. The boundary conditions for the x- and y-axes are periodic.

For the EUVL mask absorber simulation, the wavelength is 13.5 nm. The grid size of the simulations is 0.167λ. Including the boundary region, the total volume of the simulation region is $187.5\lambda \times 166.667\lambda \times 14.667\lambda$. The incident plane wave is s-polarized, with an incidence angle of 6° relative to the normal. The source is positioned at 0.5λ above the absorber. The boundary thickness on the z-axis is 4λ on each side. The absorption in other axes is realized by the PBL with the thickness of 2λ. The absorber of the EUVL mask is TaN with the RI $N = 0.9385 + 0.03776i$.

For the ODT simulations, the wavelength is 532 nm. The grid size of the simulations is 0.2λ. Including the boundary region, the total volume of the simulation region is $56.4\lambda \times 56.4\lambda \times 27\lambda$. The samples are normally illuminated with an x-polarized incident field. The source is positioned at $z = 15.4\lambda$. The boundary thickness on the z-axis is 5λ on each side. The period boundary condition is applied in the other directions. The RI of the red blood cell is obtained from a publicly available repository[25].

Data availability

The data underlying the results presented in this paper are not publicly available at this time but may be obtained from the authors upon reasonable request.

Code availability

The code are not publicly available at this time but may be obtained from the authors upon reasonable request.

Received: 11 July 2024; Accepted: 18 November 2024;
Published online: 25 November 2024

References

1. Ji, W. et al. Recent advances in metasurface design and quantum optics applications with machine learning, physics-informed neural networks, and topology optimization methods. *Light Sci. Appl.* **12**, 169 (2023).
2. Eschen, W. et al. Material-specific high-resolution table-top extreme ultraviolet microscopy. *Light Sci. Appl.* **11**, 117 (2022).
3. Vicentini, E., Wang, Z., Van Gasse, K., Hänsch, T. W. & Picqué, N. Dual-comb hyperspectral digital holography. *Nat. Photonics* **15**, 890–894 (2021).
4. Yee, K. Numerical solution of initial boundary value problems involving maxwell's equations in isotropic media. *IEEE Trans. Antennas Propag.* **14**, 302–307 (1966).
5. Teixeira, F. L. et al. Finite-difference time-domain methods. *Nat. Rev. Methods Prim.* **3**, 75 (2023).
6. Champagne, N. J., Berryman, J. G. & Buettner, H. FDFD: A 3D finite-difference frequency-domain code for electromagnetic induction tomography. *J. Computational Phys.* **170**, 830–848 (2001).
7. Lin, H.-C., Wang, Z. & Hsu, C. W. Fast multi-source nanophotonic simulations using augmented partial factorization. *Nat. Computational Sci.* **2**, 815–822 (2022).
8. Born, M. & Wolf, E. *Principles of optics: electromagnetic theory of propagation, interference and diffraction of light* (Elsevier, 2013).
9. Osnabrugge, G., Leedumrongwatthanakun, S. & Vellekoop, I. M. A convergent born series for solving the inhomogeneous helmholtz equation in arbitrarily large media. *J. Computational Phys.* **322**, 113–124 (2016).
10. Taflove, A., Hagness, S. C. & Piket-May, M. 9 - computational electromagnetics: The finite-difference time-domain method. In *The Electrical Engineering Handbook* (ed. CHEN, W.-K.) 629–670 (Academic Press, 2005). https://www.sciencedirect.com/science/article/pii/B9780121709600500463.
11. Zhang, C. et al. Low-loss metasurface optics down to the deep ultraviolet region. *Light. Sci. Appl.* **9**, 55 (2020).

12. Chen, M., Ren, D., Liu, H.-Y., Chowdhury, S. & Waller, L. Multi-layer born multiple-scattering model for 3D phase microscopy. *Optica* **7**, 394–403 (2020).
13. Lim, J., Ayoub, A. B., Antoine, E. E. & Psaltis, D. High-fidelity optical diffraction tomography of multiple scattering samples. *Light. Sci. Appl.* **8**, 82 (2019).
14. Park, Y., Depeursinge, C. & Popescu, G. Quantitative phase imaging in biomedicine. *Nat. Photonics* **12**, 578–589 (2018).
15. Evanschitzky, P. & Erdmann, A. Advanced EUV mask and imaging modeling. *J. Micro Nanolithogr. MEMS MOEMS* **16**, 041005 (2017).
16. Kang, C. et al. Large-scale photonic inverse design: computational challenges and breakthroughs. *Nanophotonics*, https://doi.org/10.1515/nanoph-2024-0127 (2024).
17. Harrington, R. F. *Wire Antennas and Seatterers*, 62–81 (Oxford University Press, Inc., 1993).
18. Houle, J. E. & Sullivan, D. M. *Electromagnetic simulation using the FDTD method with Python* (John Wiley & Sons, 2020).
19. Berenger, J.-P. A perfectly matched layer for the absorption of electromagnetic waves. *J. Computational Phys.* **114**, 185–200 (1994).
20. Shin, W. & Fan, S. Choice of the perfectly matched layer boundary condition for frequency-domain maxwell's equations solvers. *J. Computational Phys.* **231**, 3406–3431 (2012).
21. Hagstrom, T. Radiation boundary conditions for the numerical simulation of waves. *Acta Numerica* **8**, 47–106 (1999).
22. Vettenburg, T., Horsley, S. A. R. & Bertolotti, J. Calculating coherent light-wave propagation in large heterogeneous media. *Opt. Express* **27**, 11946–11967 (2019).
23. Osnabrugge, G., Benedictus, M. & Vellekoop, I. M. Ultra-thin boundary layer for high-accuracy simulations of light propagation. *Opt. Express* **29**, 1649–1658 (2021).
24. Mattes, L. & Kofuji, S. Overcoming the GPU memory limitation on FDTD through the use of overlapping subgrids. In *2010 International Conference on Microwave and Millimeter Wave Technology*, 1536–1539 (IEEE, 2010).
25. Lee, M., Hugonnet, H. & Park, Y. Inverse problem solver for multiple light scattering using modified born series. *Optica* **9**, 177–182 (2022).
26. Krüger, B., Brenner, T. & Kienle, A. Solution of the inhomogeneous Maxwell's equations using a Born series. *Opt. Express* **25**, 25165–25182 (2017).
27. Moser, S., Jesacher, A. & Ritsch-Marte, M. Efficient and accurate intensity diffraction tomography of multiple-scattering samples. *Opt. Express* **31**, 18274–18289 (2023).
28. He, P. et al. EUV mask model based on modified born series. *Opt. Express* **31**, 27797–27809 (2023).
29. He, P., Liu, J., Gu, H., Jiang, H. & Liu, S. Linearized EUV mask optimization based on the adjoint method. *Opt. Express* **32**, 8415–8424 (2024).
30. Erdmann, A. et al. Characterization and mitigation of 3D mask effects in extreme ultraviolet lithography. *Adv. Optical Technol.* **6**, 187–201 (2017).
31. Roesch, M. et al. High-NA mask phase-effects studied by AIMS EUV. In *Optical and EUV Nanolithography XXXVII*, vol. 12953, 129531F (ed. Burkhardt, M.) International Society for Optics and Photonics (SPIE, 2024). https://doi.org/10.1117/12.3010001.
32. Pang, L. Inverse lithography technology: 30 years from concept to practical, full-chip reality. *J. Micro Nanopatterning Mater. Metrol.* **20**, 030901 (2021).
33. Horstmeyer, R., Chung, J., Ou, X., Zheng, G. & Yang, C. Diffraction tomography with fourier ptychography. *Optica* **3**, 827–835 (2016).
34. Kanmaz, T. B., Ozturk, E., Demir, H. V. & Gunduz-Demir, C. Deep-learning-enabled electromagnetic near-field prediction and inverse design of metasurfaces. *Optica* **10**, 1373–1382 (2023).
35. Badawe, M. E., Almoneef, T. S. & Ramahi, O. M. A true metasurface antenna. *Sci. Rep.* **6**, 19268 (2016).
36. Yoon, J. et al. Label-free characterization of white blood cells by measuring 3D refractive index maps. *Biomed. Opt. Express* **6**, 3865–3875 (2015).
37. Park, Y. et al. Refractive index maps and membrane dynamics of human red blood cells parasitized by plasmodium falciparum. *Proc. Natl Acad. Sci.* **105**, 13730–13735 (2008).
38. Kim, K. et al. Three-dimensional label-free imaging and quantification of lipid droplets in live hepatocytes. *Sci. Rep.* **6**, 36815 (2016).
39. Cooper, K. L. et al. Multiple phases of chondrocyte enlargement underlie differences in skeletal proportions. *Nature* **495**, 375–378 (2013).
40. Zuo, C., Sun, J., Li, J., Asundi, A. & Chen, Q. Wide-field high-resolution 3D microscopy with fourier ptychographic diffraction tomography. *Opt. Lasers Eng.* **128**, 106003 (2020).
41. Hugonnet, H. et al. Multiscale label-free volumetric holographic histopathology of thick-tissue slides with subcellular resolution. *Adv. Photonics* **3**, 026004 (2021).
42. Frigo, M. & Johnson, S. FFTW: an adaptive software architecture for the FFT. In *Proceedings of the 1998 IEEE International Conference on Acoustics, Speech and Signal Processing, ICASSP '98 (Cat. No.98CH36181)*, vol. 3, 1381–1384 vol.3 (1998).
43. Gibson, W. C.*The method of moments in electromagnetics* (Chapman and Hall/CRC, Boca Raton, FL, USA, 2021).
44. Taflove, A., Oskooi, A. & Johnson, S. G. *Advances in FDTD computational electrodynamics: photonics and nanotechnology* (Artech House, 2013).
45. Liu, Q. H. The PSTD algorithm: A time-domain method requiring only two cells per wavelength. *Microw. Optical Technol. Lett.* **15**, 158–165 (1997).
46. Furht, B. (ed.). *SIMD (Single Instruction Multiple Data Processing)*, 817–819 (Springer US, 2008). https://doi.org/10.1007/978-0-387-78414-4_220
47. Demmel, J. W. *Applied Numerical Linear Algebra* (Society for Industrial and Applied Mathematics, 1997).
48. Barrett, R. et al. *Templates for the Solution of Linear Systems: Building Blocks for Iterative Methods* (Society for Industrial and Applied Mathematics, 1994). https://epubs.siam.org/doi/abs/10.1137/1.9781611971538. https://epubs.siam.org/doi/pdf/10.1137/1.9781611971538.

Acknowledgements

This research was supported by the National Natural Science Foundation of China (52130504 and 52305577), Key Research and Development Plan of Hubei Province (2021BAA013 and 2022BAA013), Major Program (JD) of Hubei Province (2023BAA008-2), Innovation Project of Optics Valley Laboratory (OVL2023PY003), and Postdoctoral Fellowship Program (Grade B) of China Postdoctoral Science Foundation (GZB20230244). The authors are grateful for the technical support from the Experiment Centre for Advanced Manufacturing and Technology in the School of Mechanical Science and Engineering of HUST. The computations were completed on the HPC Platform of Huazhong University of Science and Technology.

Author contributions

P.H. wrote the VBC codes, performed the simulations, and conducted the data analysis. J.L., H.G., H.J. and S.L. developed the theory and provided suggestions for research. S.L conceived and supervised the project. All authors contributed to designing the systems, discussing the results and preparing the manuscript.

Competing interests

The authors declare no competing interests.

Additional information

Supplementary information The online version contains supplementary material available at https://doi.org/10.1038/s42005-024-01882-5.

Correspondence and requests for materials should be addressed to Jiamin Liu or Shiyuan Liu.

Peer review information *Communications Physics* thanks Moosung Lee and the other, anonymous, reviewer(s) for their contribution to the peer review of this work. A peer review file is available.